$^{12}C(\gamma,n)$ cross section from 30 to 100 MeV

P. D. Harty,* M. N. Thompson, G. J. O'Keefe, and R. P. Rassool
School of Physics, The University of Melbourne, Parkville 3052, Australia

K. Mori, Y. Fujii, T. Suda, I. Nomura, O. Konno, T. Terasawa, and Y. Torizuka
Laboratory of Nuclear Science, Tohoku University, Mikamine, Sendai 982, Japan
(Received 30 June 1987)

This paper reports a measurement of the differential photoneutron cross section of ^{12}C at 65°, between $E_\gamma = 30$ and 100 MeV. Tagged photons, monochromatic to within 2.6 MeV, were used, thus allowing the cross sections to a wide range of final states to be observed. The results are compared to the photoproton cross section of ^{12}C, which was measured previously, under similar conditions. Comparisons are also made with calculations based on the quasi-deuteron model, and with calculations by Gari and Hebach, and Cavinato *et al.* These latter calculations incorporate two-body effects by the inclusion of meson exchange currents. The agreement between these calculations and the measured cross section is in contrast to predictions of a direct, single-nucleon knockout model of the reaction mechanism, indicating the importance of two-body effects in the photoreaction process for energies greater than 50 MeV.

I. INTRODUCTION

In the photon energy region above the giant dipole resonance (GDR) but below the photopion threshold, the mechanism responsible for photon absorption is not well understood. Collective excitations of the nucleus to particle-hole states are expected to progressively diminish in importance with increasing photon energy. In their place, photon interactions with one or two nucleons can be expected to become more significant. Clues to the relative importance of one-body and two-body effects are provided by two important characteristics of measured cross sections above the GDR. These are: (i) the comparable sizes of (γ,n_0) and (γ,p_0) cross sections, and (ii) the dominance of (γ,pn) reactions between $E_\gamma = 40$ and 140 MeV. Both of these experimental observations indicate that two-body effects play an important role in the photoreaction process.

A model based on one-body effects is the direct, single-nucleon knockout model. This has been successful in predicing the absolute cross sections and angular distributions of (γ,p_0) reactions between $E_\gamma = 60$ and 100 MeV.[1,2] For these reactions there is a large mismatch between the momentum of the photon and the ejected nucleon, providing sensitivity to high-momentum, short-range effects in nuclei. This characteristic has been exploited at Glasgow and MIT[3] in deducing momentum distributions of high-momentum, outer-shell protons inside a nucleus, from (γ,p_0) data.

At energies above $E_\gamma = 100$ MeV, the absolute cross sections of (γ,p_0) reactions are not well predicted by the direct, single-nucleon knockout model. This has generally been explained by the deficiency of high-momentum components in the wave functions calculated from shell-model potentials, such as that by Elton and Swift.[4] Such a potential averages over all short-range effects of two-nucleon interactions.

Although the direct, single-nucleon knockout model has successfully described (γ,p_0) cross sections between $E_\gamma = 60$ and 100 MeV, it has failed to account for the cross sections of (γ,n_0) reactions. The model predicts (γ,n_0) cross sections that are much smaller than corresponding (γ,p_0) cross sections. This is because the photon interacts relatively weakly with the neutron via its magnetic moment, or with the charge in the remaining $(A-1)$ residual nucleus.[2] This model also fails to account for the large (γ,pn) cross section above $E_\gamma = 40$ MeV.

On the other hand, models incorporating two-body effects have been successful in accounting for both of the above-mentioned characteristics of measured cross sections. One of these is the quasi-deuteron model (QDM), which has been applied in two different forms. In the original form, the photon is absorbed by a neutron-proton pair, with both outgoing nucleons leaving the nucleus.[5,6] This model simulates the knockout mechanism of the true final-state interactions, since it predicts similar energies for the outgoing proton and neutron, based on the deuteron photodisintegration. A detailed treatment of the kinematics has been given by Matthews *et al.*[7] This form of the QDM was applied, with some success, by Schier and Schoch[8] to $^{12}C(\gamma,n)$ and $^{16}O(\gamma,n)$ cross section data they measured for $E_\gamma = 60$–160 MeV. Likewise, McGeorge *et al.*,[9] at Mainz, applied this QDM and accounted for their tagged-photon data on the $^{12}C(\gamma,p)$ cross section, for $E_\gamma = 60$ and 80 MeV, over proton angles from 30° to 135°. These results were in agreement with similar $^{12}C(\gamma,p)$ cross section data for $E_\gamma = 45$ to 100 MeV, collected at Tohoku University,[10] using the same tagged-photon system as will be described in this paper. A number of experiments by other authors[11–23] as well have indicated the validity of the QDM.

A modified form of the QDM was proposed by

Schoch,[24] in which one of the outgoing nucleons from the neutron-proton pair is reabsorbed into the recoiling nucleus. This version of the QDM is therefore applicable to (γ,p_0) and (γ,n_0) reactions. Calculations based on this model have been able to approximately reproduce the relative magnitudes and angular dependence of available (γ,p_0) and (γ,n_0) data.[24–27] However, for a more fundamental understanding of the mechanism of photon absorption in this energy region, more microscopic models are required.

Such calculations are those of Gari and Hebach,[28] and the random-phase-approximation (RPA) calculations of Cavinato *et al.*[29] These calculations, which will be described in a later section, incorporate the effects of meson-exchange currents (MEC) and correlations in nuclear states. The two-body effects are included by the MEC, which dominate for energies above $E_\gamma = 60$ MeV, reproducing the similarity of (γ,p) and (γ,n) cross sections.

It is evident from some of the published work on cross sections between the GDR and pion threshold[1–38] that there is a shortage of high resolution data with which to evaluate the theories. Most of the cross-section measurements have been restricted to reactions leading to the ground and low-lying excited states of the residual nucleus. This is a result of the limitations associated with bremsstrahlung beams.

The aim of the present paper is to provide high-resolution $^{12}C(\gamma,n)$ data with which to compare existing $^{12}C(\gamma,p)$ data and various theoretical predictions. The most remarkable feature of the present measurement is that it was made using a tagged-photon beam. The monochromaticity obtained using tagged-photon techniques allows simultaneous determination of cross sections over a wide range of photon energies for reactions leaving the residual nuclear system in many possible states, including those of high excitations. This type of data has previously been unavailable for (γ,n) reactions. The results obtained are compared to the theoretical predictions of Gari and Hebach,[28] Cavinato *et al.*,[29] and a QDM calculation.

II. EXPERIMENT

A. Tagged photon facility

The photoneutron cross section of ^{12}C reported in this paper was measured using the tagged-photon facility at the Laboratory of Nuclear Science, Tohoku University. Details of this facility have been described previously.[39] In order to obtain a photon beam of high duty factor, a 130-MeV electron beam is injected into the 150-MeV pulsed beam stretcher. The extracted beam has a duty factor of approximately 80%, with an energy spread of only 0.2%. This beam is directed to the tagging spectrometer.

The experimental arrangement is shown in Fig. 1. At the entrance of the tagging magnet, the incident beam impinges onto a thin gold bremsstrahlung radiator. The associated recoil electrons are deflected by the tagging magnet and detected by an array of 32 electron detectors

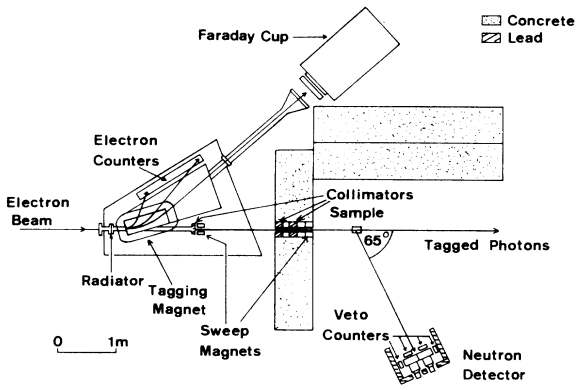

FIG. 1. The experimental arrangement for the $^{12}C(\gamma,n)$ measurement.

placed at the focal plane of the spectrometer. These plastic-scintillator detectors have widths selected to provide an energy acceptance of 2.6 MeV for each electron channel. For six channels associated with the lowest-energy photons, the width of plastic scintillator was reduced in order to decrease the energy acceptance to about 1 MeV. This improved the resolution for these channels, and consequently that of the low-energy region of the cross section. For the electron channels associated with higher energy photons, the energy acceptance of 2.6 MeV was adequate, since the resolution of the observed neutron spectra at higher photon energies was limited by the timing of the neutron flight time. Tagged photons were available with energies from 25.2 MeV up to 102 MeV, in steps of about 2.6 MeV.

At the target position, approximately 1.5 meters downstream from the tagging spectrometer, the collimated beam diameter was 40 mm. Sweep magnets were placed directly after the collimators in order to remove secondary electrons from the beam. The natural-carbon graphite sample was in the form of a cylinder, 70 mm in diameter and 100 mm in length. The tagged-photon flux was determined from the number of tagged electrons detected at the focal plane of the spectrometer. The ratio of the number of tagged photons in the beam incident on the sample to the number of electron counts (the tagging efficiency) was measured using a large lead-glass Cherenkov detector in the path of the collimated beam. This ratio was found to be 0.50 ± 3 %, and agrees with the result of a Monte Carlo calculation,[39] which took into account effects due to collimation, multiple scattering, background, Møller scattering, and the bremsstrahlung angular distribution.

B. The neutron detector

The neutron time-of-flight spectrometer used a liquid-scintillator detector placed at an angle of 65° to the beam direction at a distance of 2.64 meters from the sample position. The neutron detector consisted of 4 cells of NE213 liquid scintillator, each 18 cm in diam by 10.3 cm deep. The scintillator was contained in 24-cm square aluminum containers, the inside surfaces of which were painted with NE562 reflective paint for improved

light collection efficiency. The scintillator in each cell was viewed by a fast 13-cm-diam photomultiplier tube (Hamamatsu R1250), optically coupled to the glass window covering each cell. The cells were arranged to form a square of sides 48 cm, and were enclosed in an aluminum casing. The solid angle subtended to the sample by this neutron detector was 14.6 msr.

The top, sides, and back of the detector were shielded with 5 cm of lead, in order to reduce background radiation. Plastic scintillator "veto" counters were placed on the top, sides, and front of the detector to identify and reject pulses due to particles such as photons, electrons, and cosmic rays, which might enter the neutron detector.

C. Pulse shape discrimination

Pulses induced in the neutron detector by gamma rays were identified using "pulse shape discrimination" (PSD). A PSD module of the "zero-crossing" variety (Canberra CI 2160)[40] was used to produce timing pulses, the delays of which were proportional to the decay times of the input signals. This enabled identification of neutron- and electron-induced pulses, which have different decay times. In NE213, pulses due to highly ionizing particles, such as protons, α-particles, and ^{12}C resulting from neutron interactions in the scintillator, have longer decay times than electron-induced pulses of similar height. The decay times are, however, energy dependent.[41] Thus it was necessary to record the pulse-height information for each event, in order to more effectively distinguish between neutron- and electron-induced pulses. Without this extra information, many high-energy neutron pulses could not be distinguished from low-energy electron pulses, due to the similarity of the pulse decay times.

D. Detector efficiency

The detection efficiency of the neutron detector was calculated using a code called TOTEFF.[42] Using experimental cross sections, this analytical calculation takes into account scattering of neutrons by protons, and the reactions (n,α), (n,n'3α), (n,p), and (n,n'γ) on ^{12}C. This calculated detection efficiency was checked experimentally using quasi-monochromatic neutrons from the reaction $^{7}Li(p,n)$. Neutrons with energies of 22.95 and 38.4 MeV were produced by bombarding a 15.7 mg cm^{-2} sample of ^{7}Li with protons of energies 24.6 and 40.05 MeV, respectively, using the Tohoku University cyclotron. The efficiency determined in this way agreed within the 7% experimental error, with those calculated.

A further check on the neutron-detection efficiency was made using the $^{2}H(\gamma,n)p$ reaction, with the tagged-photon system as the source of photons. A container of heavy water was used as the sample, with the neutron detector positioned at a laboratory angle of 65°. For photon energies below about 32 MeV, the neutrons emitted following the deuteron photodisintegration have higher energies than those from the $^{16}O(\gamma,n)$ reaction. For the lowest tagged-photon energies (25.2 and 27.2 MeV) the neutron peaks at $E_n = 12.2$ and 13.2 MeV from the deuteron photodisintegration were clearly resolved from the $^{16}O(\gamma,n_0)$ peaks, at 9.0 and 10.9 MeV, respectively. The neutron-detection efficiencies at these energies were estimated using the differential $^{2}H(\gamma,n)p$ cross section at 65°, as calculated by Partovi.[43] This theoretical cross section has been shown to agree with existing experimental data within 7%.[44,45] Overall, in view of the above experimental checks, the uncertainty in the neutron efficiency was calculated to be 7%.

E. Detector threshold

Not all pulses due to neutrons interacting in the detector are large enough to be distinguished from noise pulses. Thus the neutron-detection efficiency depends on the threshold setting of the detector electronics. The measured and calculated efficiencies were obtained for a threshold energy of 3.0 MeV equivalent-electron-energy (i.e., the pulse height corresponding to that produced by 3.0 MeV electrons). From the relative response of the NE213 scintillator to protons and electrons, as measured by Verbinski *et al.*,[46] this corresponds to a neutron energy threshold of about 7 MeV. This threshold energy was chosen in order to obtain good PSD separation characteristics up to the maximum neutron energy of 77 MeV, and to discriminate against many of the large number of low-energy background neutrons and gamma rays. This background is produced by electronuclear reactions involving electrons from the incident beam which did not produce bremsstrahlung, and which subsequently hit the Faraday cup. Although most of these low-energy neutrons and gamma rays are stopped by the shielding, enough reach the neutron detector to cause a background problem if the detection threshold is set too low.

F. Neutron energies and resolution

For the present measurement of the $^{12}C(\gamma,n)$ cross section, the energies of detected neutrons ranged from 7 to 77 MeV, corresponding to times of flight (TOF) between 73 and 23 ns. The coincidence timing resolution between neutron-detector pulses and electron-detector pulses was 1.4 ns FWHM, which limited the neutron energy resolution, especially for high-energy neutrons. The neutron energy resolution for spectra generated by photons, monochromatic to 2.6 MeV, i.e., for tagging channels 1–26, is shown in Table I. Table II gives similar data for tagging channels 27–32, those electron detectors which were modified as described earlier, in order to resolve finer detail in the cross section.

The data were collected event by event using 32 time-to-digital converters (TDC) to record the times between neutron and correlated electron pulses. To ensure that a neutron pulse starts the TDC interval, the electron pulses were delayed by a fixed interval so as to occur after any associated neutron pulse. This significantly reduced the deadtime by confining the operation of the TDC's to events where a neutron-detector pulse was detected.

The TDC spectra each contained a sharp peak corre-

TABLE I. Neutron energy resolution for spectra generated by photons, monochromatic to 2.6 MeV (i.e., photons with tagging electrons in channels 1–26).

Neutron energy (MeV)	Resolution (FWHM) (MeV)	% resolution
10	1.9	19.0
20	2.3	11.5
30	3.1	10.3
40	4.2	10.5
50	5.5	11.0
60	6.9	11.5
70	8.5	12.1
80	10.2	12.8

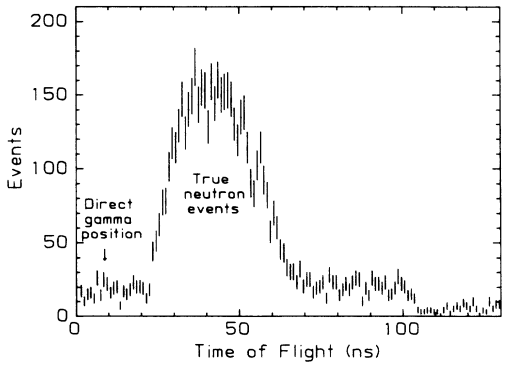

FIG. 2. The combined TOF spectrum for all 32 electron channels. The features of the spectrum are described in the text.

sponding to tagged photons scattered from the ^{12}C sample. This peak had a width corresponding to the 1.4 ns timing resolution of the tagging coincidence. The position of this gamma-ray TOF peak provided a timing calibration which enabled the TDC spectra to be converted to TOF spectra.

The combined TOF spectrum for all 32 electron channels is shown in Fig. 2. Gamma-ray and electron events have been discriminated out by PSD, allowing the electron-correlated neutron events to be clearly observed in a 50 ns region of interest (23–73 ns). The counts observed on each side of these neutron events were due to random electron-detector pulses occurring inside the 108-ns-long coincidence timing gate. These counts constituted a background that was fitted by a horizontal line. The magnitude of this background is dependent on the duty factor and the detected-electron rate, which was limited to 5.2×10^5 electron s^{-1} during the experiment, in order to maintain an acceptably low rate of accidental coincidences.

Of the random coincidences seen in Fig. 2, it is estimated that 12% were initiated by cosmic rays, and 18% by true neutron events that were "double tagged." The remaining 70% were due to uncorrelated low-energy neutrons, mostly produced by electronuclear reactions at the Faraday cup. These random coincidences constitute a background that is 19.6% of the total counts in the 50-ns region of interest. Thus the average signal-to-noise ratio was 5.1:1.

TABLE II. Neutron energy resolution for spectra generated by photons, monochromatic to 1 MeV (i.e., photons with tagging electrons in channels 27–32). These channels were modified as described in the text, in order to improve the photon energy resolution.

Neutron energy (MeV)	Resolution (FWHM) (MeV)	% resolution
7	0.88	12.6
10	0.98	9.8
13	1.13	8.7
16	1.32	8.3

After subtraction of the background due to random coincidences, neutron-energy spectra were constructed from the TOF spectra, using the known flight-path length. A sample spectrum is shown in Fig. 3 for a photon energy of 33.7±0.5 MeV. For photons of this energy, ground-state neutrons emitted at 65° have an energy of 13.9 MeV, while those leaving ^{11}C in its first excited state have an energy of 12.0 MeV. These energies are marked in the figure by arrows, where peaks can be seen with widths corresponding to the calculated energy-resolution values of Table II.

Similarly, for the other tagged-photon channels, neutron peaks occur at energies corresponding to reactions leaving ^{11}C in its ground and low-lying excited states. In order to facilitate the correlation of peaks in the experimental spectra with levels in the residual ^{11}C nucleus, it is convenient to plot the neutron spectra using a scale of "residual excitation energy," E_x. This is defined as

$$E_x = E_\gamma - E_n - E_{\text{recoil}} - Q \ , \tag{1}$$

where E_γ is the incident tagged-photon energy, E_n is the neutron energy, E_{recoil} is the kinetic energy of the recoil-

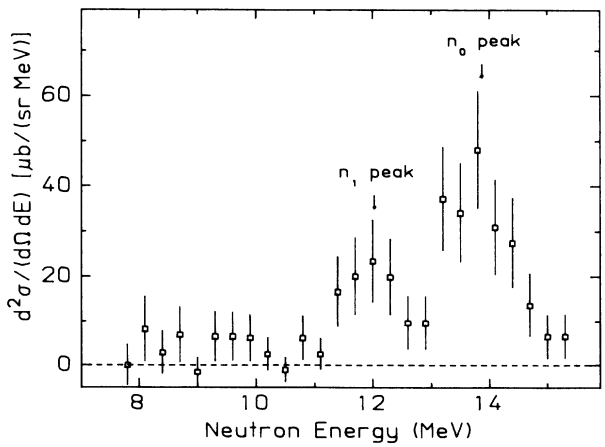

FIG. 3. The neutron energy spectrum for photons tagged by electron channel 28, corresponding to $E_\gamma = 33.7\pm0.5$ MeV. The arrows mark the energies of neutrons that leave ^{11}C in its ground and first excited states.

ing nucleus, and Q is the Q-value of the reaction, which for the $^{12}C(\gamma,n)$ reaction is 18.7 MeV.

G. The absolute cross section scale

The absolute differential cross section is given by

$$\frac{d\sigma}{d\Omega_n} = \frac{\text{neutron yield}}{N_C d\Omega N_\gamma \xi(E_n)\eta(E_n)} , \quad (2)$$

where N_C is the effective number of ^{12}C nuclei per cm^2. This was calculated from the effective sample thickness, which varied from 15.02 to 15.07 g cm^{-2} over the range of incident photon energies. The solid angle of the neutron detector $d\Omega$ was 14.6 msr. The number of tagged photons incident on the sample N_γ was calculated from the product of the tagging efficiency and electron counts. The neutron-detection efficiency for each neutron energy, given by $\xi(E_n)$, was determined by the theoretical code described above.

The neutron-attenuation factor, $\eta(E_n)$, makes a correction for losses in the neutron flux due to scattering. For zero scattering this factor is unity. The main contribution is inelastic scattering off ^{12}C nuclei in the sample; however, there is also inelastic scattering off ^{14}N and ^{16}O nuclei in the air, and scattering off ^{12}C and protons in the plastic scintillator "veto" counters. The effect of inelastic scattering in the sample was estimated using a Monte Carlo routine,[47] which assumed that the inelastically-scattered neutrons were undetected. No correction was made for the effects of elastic scattering off ^{12}C, based on the assumption that approximately equal numbers of neutrons would scatter "into" and "out of" the detection solid angle. This is consistent with the observations of Drosg[48] for samples of CH_2 of smaller, but comparable dimensions to the graphite sample used in this experiment. The uncertainty introduced by this approximate treatment is estimated to be about 6%.

A loss of neutron flux also occurs in the plastic scintillator "veto" counters, where scattering off both ^{12}C and protons must be considered. This scattering may produce a "veto" pulse, thus electronically preventing the detection of the scattered neutron in the NE213. The plastic scintillator has similar composition to the NE213 scintillator, so that the probability of a "veto" pulse can be calculated from the known response of NE213. After correcting for the different density and detection threshold, it was calculated that the loss of flux due to the "veto" counters varied from 4.5% (for low-energy neutrons) to 3.3% (at $E_n = 80$ MeV). The total loss of flux due to scattering in the sample, air, and "veto" counters, varied from 21% (at $E_n = 15$ MeV) to 11% (at $E_n = 80$ MeV).

H. Cross section determination

In order to derive the cross sections to the ground and low-lying excited states of ^{11}C, Gaussians were fitted to the neutron spectra. The Gaussians were centered at energies of $E_x = 0$, 2.0, 4.6 (average of 4.3 and 4.8), 6.5, and 8.1 MeV, corresponding to low-lying states in ^{11}C. The states at 6.34, 6.90, 7.50, and 8.43 MeV were not fitted with separate Gaussians, since the neutron-energy resolution was not good enough to warrant such a treatment. The widths of the Gaussians were fixed by the calculated values of neutron-energy resolution, which are listed in Tables I and II.

III. RESULTS AND DISCUSSION

Four examples of the photoneutron spectra obtained in this experiment are shown in Fig. 4. These spectra are for photon energies of $E_\gamma = 33.7$, 47.6, 60.5, and 74.8 MeV, respectively. The energy bins used for these spectra were chosen to provide a meaningful display of the data with regard to resolution and statistics. The solid

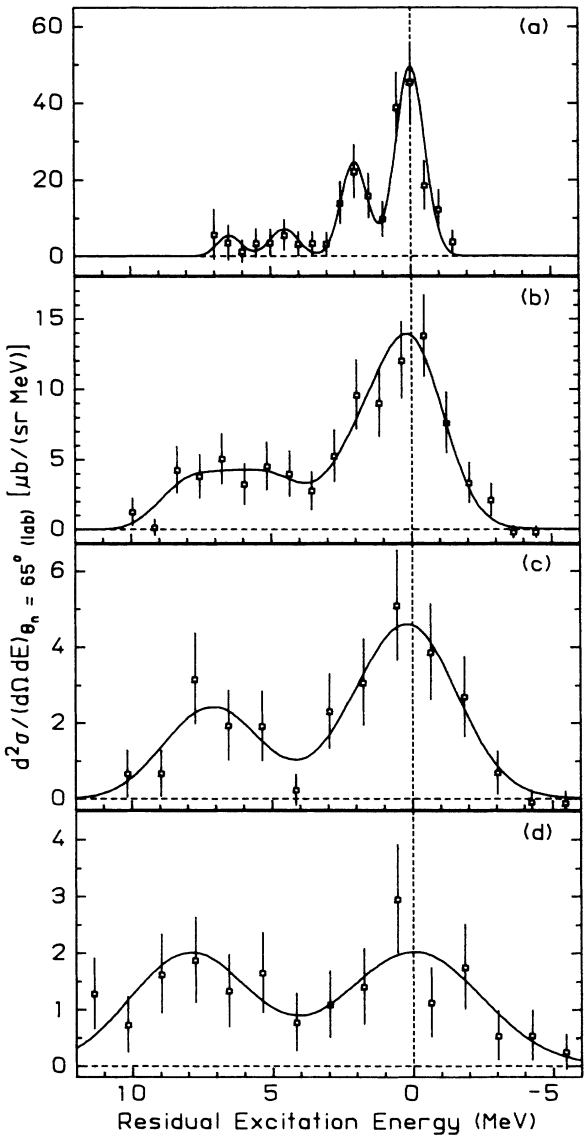

FIG. 4. Four examples of the experimental photoneutron spectra, shown up to $E_x = 10$ MeV. The spectra are for photon energies of: (a) 33.7±0.5 MeV, (b) 47.6±1.3 MeV, (c) 60.5±1.3 MeV, and (d) 74.8±2.6 MeV. The solid curves represent the Gaussians that were fitted to the spectra, as described in the text.

lines represent the Gaussians, fitted as described above. It is clearly seen from these examples that the spectra exhibit structure consistent with population of the ground and low-lying excited states of ^{11}C. It is evident that the resolution does not allow an accurate estimate of the cross sections to specific single final states of ^{11}C. For this reason, only the cross sections for the reactions $^{12}C(\gamma,n_{0,1})$ and $^{12}C(\gamma,n_{2-9})$ were determined from the fits.

These two cross sections are plotted in Figs. 5 and 6, and are listed in Tables III and IV. The errors quoted are statistical, and it should be noted that there is a system uncertainty totaling 10%. This systematic uncertainty includes errors due to the neutron-detection efficiency (7%), neutron scattering correction (6%), and tagging efficiency (3%).

The $^{12}C(\gamma,n_{0,1})$ and $^{12}C(\gamma,n_{2-9})$ cross sections shown in Figs. 5 and 6 are very similar. They both decrease fairly smoothly from below $E_\gamma=40$ MeV to about 65 MeV, where both appear to undergo a change in slope. The average slope of the $^{12}C(\gamma,n_{2-9})$ cross section over the measured region is less than that of $^{12}C(\gamma,n_{0,1})$. This indicates that the relative importance of the $^{12}C(\gamma,n_{0,1})$ cross section progressively decreases with increasing photon energy. This effect has also been observed in comparisons between photoproton cross sections [viz. $^{12}C(\gamma,p_0)$ and $^{12}C(\gamma,p_{2,3,4})$] measured at Glasgow.[33] A similar observation can be made for the cross sections to higher residual excitation energies, shown in Figs. 8, 9, and 10. It is clear that with increasing photon energy the cross sections to higher residual states become progressively more significant compared to the cross section to low-lying states. This is consistent with models that include two-body effects in the photon-absorption process. As these effects become more significant at higher energies, the relative probability of forming the more complex two-hole–one-particle residual states should increase. A corresponding increase in two-nucleon emission is also expected, since nucleon-nucleon interactions in the final state will deliver enough energy to the second nucleon for it to leave the residual nucleus. This accounts for the large cross sections at higher residual excitation energies.

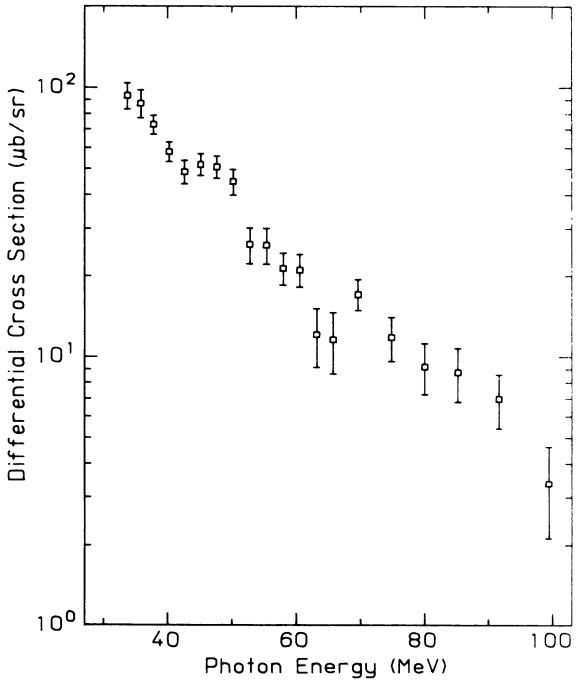

FIG. 5. The differential cross section of $^{12}C(\gamma,n_{0,1})$ in the laboratory frame, at $\theta_n=65°$. The error bars represent statistical uncertainties. There is an additional systematic uncertainty in the absolute scale, totaling 10%.

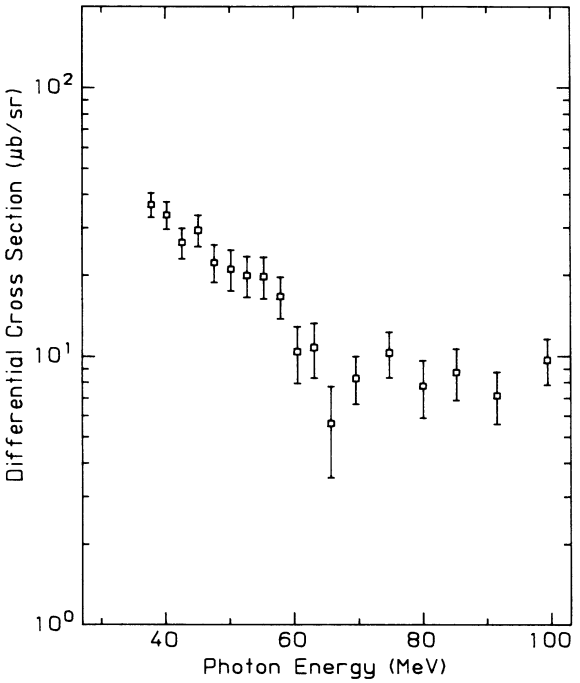

FIG. 6. The differential cross section of $^{12}C(\gamma,n_{2-9})$ in the laboratory frame, at $\theta_n=65°$. The error bars represent statistical uncertainties. There is an additional systematic uncertainty in the absolute scale, totaling 10%.

The present results for the $^{12}C(\gamma,n_{0,1})$ differential cross section are compared to the 60° datum point of Schier and Schoch[8] for the $^{12}C(\gamma,n_0)$ cross section in Fig. 7. This point, which was measured at Mainz, lies about 30% lower than the present data, but this is expected since the Mainz datum does not include the $^{12}C(\gamma,n_1)$ cross section. In the same figure, the data of Mori *et al.*[10] for the $^{12}C(\gamma,p_{0,1})$ differential cross section are shown for comparison. These data were obtained us-

TABLE III. Differential cross sections for $^{12}C(\gamma,n_0)$ and $^{12}C(\gamma,n_1)$ at $\theta_{lab}=65°$.

Photon energy (MeV)	$^{12}C(\gamma,n_0)$ $(d\sigma/d\Omega)$ (μb/sr)	$^{12}C(\gamma,n_1)$ $(d\sigma/d\Omega)$ (μb/sr)
31.2	71.0±9	
33.7	63.7±9	29.7±6
35.8	59.1±9	28.3±6

TABLE IV. Differential cross sections for $^{12}C(\gamma,n_{0,1})$ and $^{12}C(\gamma,n_{2-9})$ at $\theta_{lab}=65°$.

Photon energy (MeV)	$^{12}C(\gamma,n_{0,1})$ $(d\sigma/d\Omega)$ (μb/sr)	$^{12}C(\gamma,n_{2-9})$ $(d\sigma/d\Omega)$ (μb/sr)
33.7	93.4±11	
35.8	87.4±11	
37.8	72.8±6	36.6±4
40.2	57.9±5	33.5±4
42.6	48.7±5	26.4±4
45.1	51.9±5	29.4±4
47.6	50.8±5	22.3±4
50.2	44.8±5	21.1±4
52.7	26.2±4	20.0±4
55.3	26.1±4	19.8±4
57.9	21.4±3	16.7±3
60.5	21.1±3	10.4±3
63.1	12.1±3	10.8±3
65.7	11.6±3	5.6±2
69.6	17.1±2	8.3±2
74.8	11.8±2	10.3±2
80.0	9.2±2	7.8±2
85.2	8.8±2	8.7±2
91.6	7.0±2	7.2±2
99.4	3.4±1	9.7±2

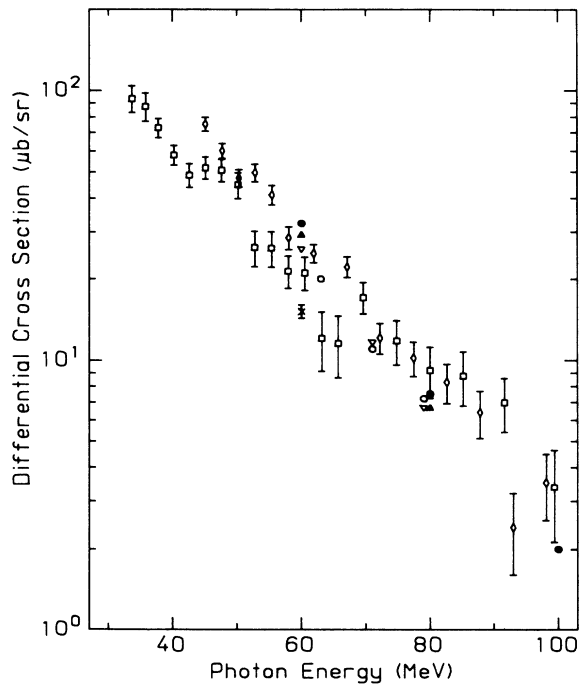

FIG. 7. The differential cross sections of $^{12}C(\gamma,n_{0,1})$ and $^{12}C(\gamma,p_{0,1})$, at $\theta_{lab}=65°$. The squares are the results of the present $^{12}C(\gamma,n_{0,1})$ measurement, and the diamonds are the $^{12}C(\gamma,p_{0,1})$ data of Mori *et al.* (Ref. 10). Both cross sections have additional systematic uncertainties totaling 10%. The cross represents the 60° datum point of Schoch *et al.* (Ref. 8), for the $^{12}C(\gamma,n_0)$ cross section. The theoretical calculations of Gari and Hebach (Ref. 28) are represented by the circles: solid circles—$^{12}C(\gamma,p_0)$, and open circles—$^{12}C(\gamma,n_0)$. The triangles represent the calculations of Cavinato *et al.* (Ref. 29): solid triangles—$^{12}C(\gamma,p_0)$, and open triangles—$^{12}C(\gamma,n_0)$.

ing the same tagged-photon facility as the present measurement. It can be seen that the $^{12}C(\gamma,n_{0,1})$ and $^{12}C(\gamma,p_{0,1})$ cross sections are very similar, especially in the region from 70 to 100 MeV.

This similarity cannot be reconciled with a direct, single-nucleon knockout model, which predicts that (γ,n_0) cross sections be relatively smaller than (γ,p_0) cross sections. In this model the photon interacts relatively weakly with the magnetic moment of the neutron or with the charge in the remaining $(A-1)$ residual nucleus. The second of these has been shown by Boffi *et al.* to produce significant contributions to the (γ,n_0) cross section,[2,49,50] especially at backward angles. A further increase in the predicted (γ,n_0) cross section occurs if charge exchange in the final state is taken into account for direct (γ,p) reactions.[51] This is a two-step process where the direct (γ,p) reaction is followed by a (p,n) reaction with the residual nucleus. Boffi *et al.*[51] have shown that this mechanism can increase the predicted (γ,n_0) cross section by about 50%. However, despite these contributions, the $^{12}C(\gamma,n_0)$ cross section predicted by this model falls well below both the corresponding $^{12}C(\gamma,p_0)$ cross section and the experimental $^{12}C(\gamma,n_0)$ cross section.

On the other hand, the similarity between the $^{12}C(\gamma,n_{0,1})$ and $^{12}C(\gamma,p_{0,1})$ cross sections is consistent with models that incorporate two-body effects in the photoreaction process. Three such models will be discussed in the following sections.

A. Models of photon absorption that include two-body effects

1. The Gari and Hebach model

The circles in Fig. 7 are the results of calculations of the $^{12}C(\gamma,n_0)$ and $^{12}C(\gamma,p_0)$ differential cross sections at 65°, by Gari and Hebach.[28] In these calculations, the effective nuclear Hamiltonian is written as the sum of a shell-model part (with a Woods-Saxon-type, single-particle potential) and residual interaction. The single-particle potential neglects Coulomb and spin-orbit contributions, and is thus the same for neutrons and protons. The residual interaction is assumed to be an effective two-body potential with a Yukawa radial dependence, and includes an exchange mixture of the Rosenfeld type.

The transition matrix was split into four separate terms, representing contributions from: (i) shell model, (ii) initial-state correlations, (iii) final-state correlations, and (iv) MEC. Contributions (i), (ii), and (iii) are associated with one-body effective nucleonic currents, whereas the MEC has many-body components, however, only the two-body terms were included in their calculations. They showed that the MEC term in the transition matrix is necessary to ensure gauge invariance.

The results of their calculations show that the MEC contribution dominates for energies above $E_\gamma=60$ MeV. Correlations in the initial and final states are of secondary importance, while the shell-model contribution is least important. The dominance of the MEC contribu-

tion explains the comparable magnitudes of the photoproton and photoneutron cross sections. As seen in Fig. 7, the cross sections calculated by Gari and Hebach reproduce well the magnitudes and slopes of the measured cross sections. However, these calculated cross sections depend sensitively on the choice of final-state potential, which for these calculations has been criticized[34,37] as being unrealistically deep. It was argued in these papers that the deep final-state potential, which was chosen to ensure orthogonality between initial and final states, depresses the shell-model contribution to the cross sections. These shell-model contributions would also be enhanced by the correct treatment of the center-of-mass motion of the $(A-1)$ nucleus, as shown by Boffi *et al.*,[2,49,50] and by Schumacher *et al.*[38]

2. *Random-phase-approximation calculations*

The triangles plotted in Fig. 7 show the results of calculations of the $^{12}C(\gamma,n_0)$ and $^{12}C(\gamma,p_0)$ differential cross sections at 65°, by Cavinato, Marangoni, Ottaviani, and Saruis.[29] As in the Gari and Hebach theory, the reaction mechanism for this self-consistent, RPA calculation is based on the excitation of intermediate particle-hole and hole-particle states. The calculations include $E1$ and $E2$ multipole transitions expressed in the long-wavelength limit.

In this theory, Hartree-Fock and RPA Hamiltonians are constructed for a Skyrme III nucleon-nucleon interaction. The MEC can arise from two sources: the particle-hole residual interaction and the Hartree-Fock field. In the Gari and Hebach theory, the first of these is the source of the MEC contributions, but in RPA theory they arise predominantly from the effective mass in the Hartree-Fock field. The exchange contributions are local and energy dependent. Moreover, MEC and correlations in nuclear states are intimately connected in this model.[29] The calculated differential cross sections agree well in magnitude and slope with the experimental data presented in Fig. 7.

3. *Quasi-deuteron model (QDM) calculations*

The similarity of the $^{12}C(\gamma,n_{0,1})$ and $^{12}C(\gamma,p_{0,1})$ cross sections can also be understood in terms of a phenomenological QDM in modified form, as developed by Schoch.[24] This form of the QDM assumes that after photodisintegration of the QD, one of the nucleons remains bound in its original state in the nucleus, accepting a momentum transfer. The emitted nucleon can therefore leave the residual nucleus in its ground state. This model predicts similar magnitudes for the $^{12}C(\gamma,n_0)$ and $^{12}C(\gamma,p_0)$ cross sections, as observed, with the $^{12}C(\gamma,p_0)$ differential cross section being more forward peaked than the $^{12}C(\gamma,n_0)$ cross section, as in the case of the corresponding deuteron photodisintegration. This latter prediction has been investigated to some extent by Schoch,[26] who plotted the ratio of the (γ,p_0) cross section to the (γ,n_0) cross section against detection angle, for ^{16}O and ^{12}C, at $E_\gamma=60$ MeV. The ratios obtained using data existing at that time generally conformed to predictions of the QDM.[26] The present ^{12}C data, at $E_\gamma=60$ MeV, and that of Mori *et al.*,[10] lead to a ratio that agrees with the QDM prediction; however, in the region from $E_\gamma=70$ to 100 MeV, the experimental ratio is close to unity, in disagreement with the QDM predictions.

B. The cross section at high missing energy

The present measurement demonstrates the power of the tagged-photon technique for measuring cross sections leading to excited residual states. The combination of monochromatic photons and good neutron resolution allows these cross sections to be determined uniquely. However, in regions of neutron spectra where neutrons from the $^{12}C(\gamma,np)$ reaction may contribute, the excitation of the residual nucleus is not uniquely determined from the neutron energy. In such cases it is more appropriate to use an energy scale of "missing energy," which includes the kinetic energy of any additional reaction product and the Q value, as well as the excitation energy of the residual nucleus. The missing energy is defined as

$$E_m=E_\gamma-E_n-E_{\text{recoil}} \tag{3}$$

where E_{recoil} is the kinetic energy of the recoiling nucleus, calculated assuming single-nucleon emission. A similar definition can be used for proton spectra. For ground-state neutrons (or protons), following (γ,n_0) [or (γ,p_0)] reactions, E_m is simply equal to the Q value of the reaction, which for $^{12}C(\gamma,n)$ is 18.7 MeV and for $^{12}C(\gamma,p)$ is 16.0 MeV. However, for $^{12}C(\gamma,np)$ reactions the Q value is 27.4 MeV, resulting in high values of E_m in the photoneutron and photoproton spectra.

The measured ^{12}C photoneutron spectra for $E_\gamma>45$ MeV are shown in Figs. 8 and 9. In view of the poor statistics, and in order to allow a more meaningful comparison with theory, data were combined from several spectra measured at different photon energies. The spectra shown in Figs. 8 and 9 are the result of summing over 10-MeV bins, centered at energies from 50 to 100 MeV.

1. *QDM calculations for the region of high missing energy*

The curves in Figs. 8 and 9 are the result of a QDM calculation, carried out using a treatment similar to that of Matthews *et al.*,[7] Schier and Schoch,[8] and McGeorge *et al.*[9] The equation used to calculate the double-differential cross section was

$$\frac{d^2\sigma}{dE_m d\Omega_n}=\frac{C'LNZ\epsilon}{A}\int d^3P F(\mathbf{P})\frac{d\sigma}{d\Omega_D}\delta(\omega_1-\omega)J_{\text{tot}}\ , \tag{4}$$

where L is the Levinger parameter and N, Z, and A are the neutron, proton, and mass numbers, respectively. The term $F(\mathbf{P})$ is the normalized neutron-proton pair momentum distribution, $\mathbf{P}$ being the momentum of the quasi-deuteron. The delta function $\delta(\omega_1-\omega)$, where ω_1 is the tagged-photon energy, replaces the usual photon spectrum term $B(\omega)$.[7] The integral then becomes an in-

tegral over the directions of **P**, with the value of **P** for each event determined by a Monte Carlo sampling of the **P** distribution. The total Jacobian J_{tot} is modified to take account of this change in dimension of the integral.[7]

The symbol ϵ in Eq. (4) is the transparency factor, taking into account the reduced number of emitted nucleons due to the strong final-state interaction. Lastly, the term C' is a constant, which ensures that the total deuteron and QD photodisintegration cross sections, integrated over all energies and angles, satisfy the relation

$$\sigma_{QD}=\frac{\epsilon LNZ}{A}\sigma_D \ . \tag{5}$$

This form of the QDM assumes that after photodisintegration of the QD, the undetected nucleon is left in an unbound state. For this reason the emitted-nucleon energies predicted by this model give rise to high values of missing energies. This version of the QDM makes no attempt to account for reactions involving single-nucleon emission. The curves in Figs. 8 and 9, therefore, do not extend into the missing-energy region corresponding to the ground and low-lying residual states of ^{11}C.

In the QDM calculations, the momentum distribution $F(\mathbf{P})$ of the neutron-proton pair was approximated by expressions calculated by Gottfried,[52] using a harmonic-oscillator potential. The equation used for $F(\mathbf{P})$ was

$$F(\mathbf{P})=\tfrac{1}{2}F_{pp}(\mathbf{P})+\tfrac{1}{2}F_{ps}(\mathbf{P}) \ , \tag{6}$$

where $F_{pp}(\mathbf{P})$ is the momentum distribution for a pair of p-shell nucleons, and $F_{ps}(\mathbf{P})$ is the momentum distribution when one nucleon is from the p shell and the other from the s shell. The forms of the separate parts were

$$F_{pp}(\mathbf{P})=\tfrac{4}{15}(2\pi\alpha^2)^{-3/2}(3-P^2/\alpha^2+P^4/4\alpha^4) \times\exp(-P^2/2\alpha^2) \ , \tag{7}$$

$$F_{ps}(\mathbf{P})=\tfrac{1}{3}(2\pi\alpha^2)^{-3/2}(P^2/\alpha^2)\exp(-P^2/2\alpha^2) \ , \tag{8}$$

where α is the harmonic-oscillator parameter and **P** is the momentum of the QD. These distributions satisfy the equation

$$\int_0^\infty F(\mathbf{P})d^3P=1 \ . \tag{9}$$

It was assumed that there would be no contribution to the cross section from a pair of s-shell nucleons, due to the much larger separation energy for such emission. For pp and ps nucleon-pair emission, the Q values were taken to be 30 MeV and 50 MeV, respectively. The

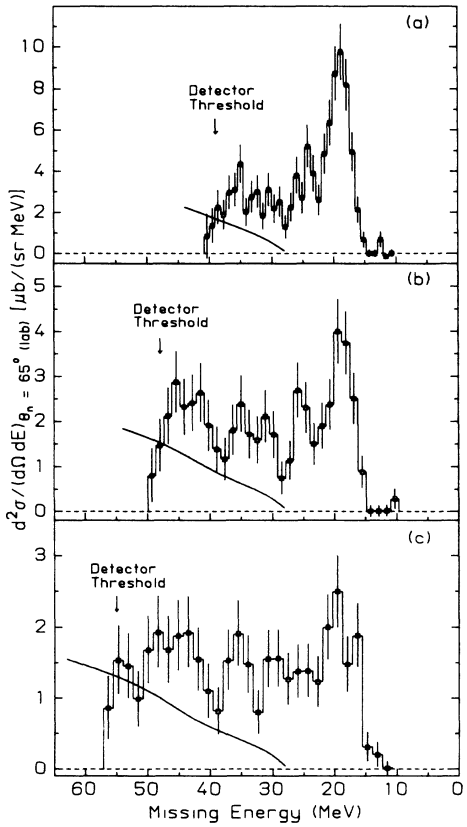

FIG. 8. The measured missing-energy spectra of the ^{12}C photoneutron cross section, at $\theta_n=65°$. The solid curves result from calculations based on a QDM, as described in the text. The spectra are for photon energy ranges of: (a) 50±5 MeV, (b) 60±5 MeV, and (c) 70±5 MeV.

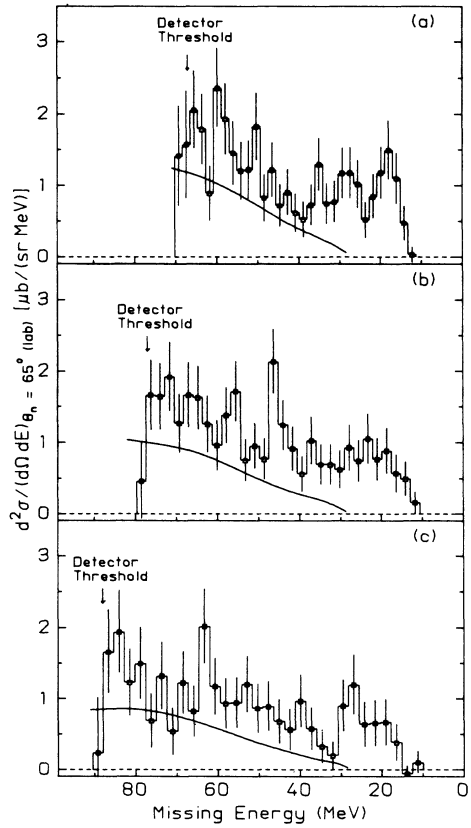

FIG. 9. As for Fig. 8, but for photon energy ranges of: (a) 80±5 MeV, (b) 90±5 MeV, and (c) 100±5 MeV.

binding energy of the QD was assumed to be -10 MeV. The values above are similar to those used by Matthews *et al.*,[7] Barton and Smith,[14] Schier and Schoch,[8] and McGeorge *et al.*,[9] in similar QDM calculations.

The value of the harmonic-oscillator parameter α was chosen to be 120 MeV/c for both shells. This value is consistent with those used by other authors.[7–9] It is also consistent with measurements of the rms radius of the ^{12}C nucleus, determined from electron-scattering data.[53,54] The value of the Levinger parameter was chosen to be $L=5.8\pm1.5$, in accordance with that obtained for ^{12}C by Tavares *et al.*[18] This is consistent with the value of $L=5$ that was obtained by Homma *et al.*[19] at higher energies. It is also consistent with the trend of measured values for mass numbers near 12, as compiled by Anghinolfi *et al.*[23]

The transparency factor ϵ was chosen with regard to previous treatments of QDM calculations. Generally, authors[3,9,23,24] have used an energy-independent factor, which is a reasonable approximation for neutrons with energies below 70 MeV.[8,55] In the present QDM calculations, a value of $\epsilon=0.45$ was used for outgoing protons and neutrons. This value is similar to that resulting from Gottfried's[52] treatment in terms of nucleon mean-free paths in the nucleus; a method also used by other authors.[7,16,17,19] The uncertainty introduced by the choice of this value is estimated to be 20%.

The QDM-calculated curves do not change significantly with parameter changes in the Q values and QD binding energy. However, the calculated curves are relatively sensitive to the choice of the harmonic-oscillator parameter α. If the value of α is changed to 90 MeV/c, the curves increase in magnitude by about 20% over the region from $E_m=30$ to 70 MeV. This is a similar effect to that seen by Blann *et al.*[56] for photoneutron spectra predicted by a precompound-decay model, when they varied the energy limitation of the correlated hole pair left behind.

It can be seen in Figs. 8 and 9 that the curves representing the results of the QDM calculations reproduce well the shape of the photoneutron spectra in the region of high missing energy. Over the range from $E_m=30$ to 50 MeV, the QDM-calculated curves account for about 40% of the measured cross section. Over the range from $E_m=50$ to 70 MeV, this increases to 60%. This approximate agreement indicates that in the region of high missing energy, the ^{12}C(γ,np) reaction is the major contributor to the experimental spectra. The large cross section at low missing energy suggests that the ^{12}C(γ,n) reaction involving single neutron emission is also important for photon energies up to 100 MeV.

The ^{12}C photoneutron spectra in Figs. 8 and 9 cannot be explained by a direct, single-nucleon knockout model. For single-nucleon emission, the highest missing energy occurs when a nucleon from the 1s-shell is emitted. From the evidence of quasi-free scattering experiments such as ^{12}C(p,2p),[57] a peak due to 1s-shell emission might be expected at $E_m\approx36$ MeV, with a width of approximately 13 MeV. However, there is no evidence of such a peak in the experimental spectra in Figs. 8 and 9. The large cross section at energies far above $E_m=36$ MeV must therefore be explained in terms of a different reaction mechanism; one that involves the emission of at least two nucleons.

Similar results to those reported here have been obtained at Tohoku University[10] and at Mainz,[9] measuring photoprotons emitted from ^{12}C. The results from Tohoku University have been reproduced in Fig. 10. The solid curves show the prediction of the QDM for the ^{12}C photoproton spectra. At high missing energy there is agreement in shape, similar to that obtained for the photoneutron data. Over the range from $E_m=30$ to 50 MeV, the QDM-calculated curves account for about 60% of the measured cross section. This is higher than the 40% accounted for in the photoneutron spectra over the corresponding missing energy region. This can be explained by the dependence of the QDM calculations on the deuteron photodisintegration cross section, for which the angular distribution of emitted protons is more forward peaked than that of the neutrons. However, this will not necessarily apply to the photoproton and

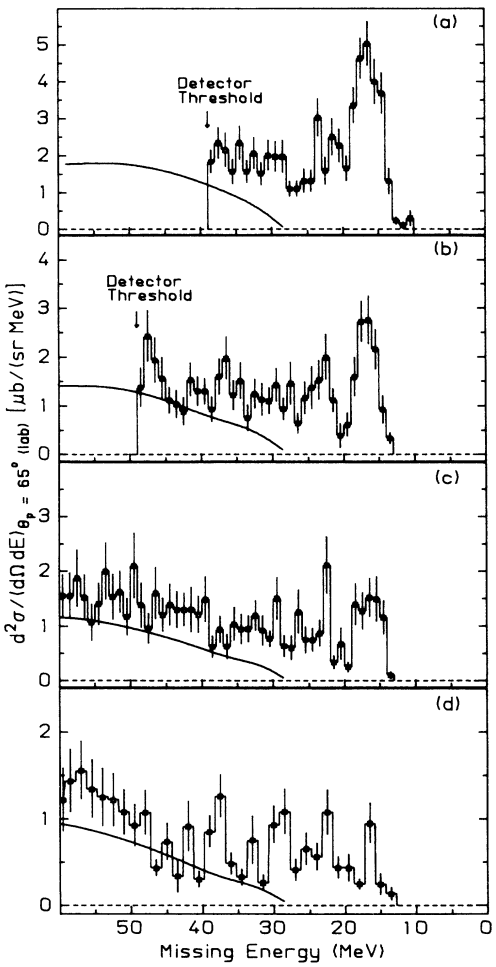

FIG. 10. The measured missing-energy spectra of the ^{12}C photoproton cross section, at $\theta_p=65°$, as measured by Mori *et al.* (Ref. 10). The solid curves result from calculations based on a QDM, as described in the text. The spectra are for photon energy ranges of: (a) 65±5 MeV, (b) 75±5 MeV, (c) 85±5 MeV, and (d) 95±5 MeV.

photoneutron spectra of a more complex nucleus like ^{12}C.

The present ^{12}C photoneutron cross section shown in Figs. 8 and 9 shows features that are in agreement with the ^{12}C photoproton data of Mori *et al.*,[10] shown in Fig. 10, and also the ^{12}C photoproton data of McGeorge *et al.*[9] The magnitudes of these measured cross sections agree within errors over the entire range of missing energy. This agreement emphasizes the importance of two-body effects in the photoreaction process over the photon energy range above about 50 MeV.

IV. SUMMARY AND CONCLUSIONS

The tagged-photon technique has been employed in measuring the ^{12}C photoneutron cross section at $\theta_n = 65°$ for $E_\gamma = 30$ to 100 MeV. The use of a high-resolution neutron TOF spectrometer allowed the measurement of the cross section to selective excitation energy regions in the residual system.

At low residual excitation energies, the $^{12}C(\gamma,n_{0,1})$ and $^{12}C(\gamma,n_{2-9})$ differential cross sections were extracted from the data. These two cross sections are seen to decrease smoothly with photon energy, except for a small change in slope that seems to occur at $E_\gamma = 65$ MeV. The smaller rate of decrease for the $^{12}C(\gamma,n_{2-9})$ cross section shows the increasing relative importance of the cross section to higher residual excitation energies, as the photon energy increases. This seems to indicate an increased relative probability of forming the more complex two-hole–one-particle residual states, as the photon energy increases. This might well be expected if two-body effects in the photoreaction processes are progressively increasing over the photon energy range.

A comparison of the $^{12}C(\gamma,n_{0,1})$ differential cross section to that of $^{12}C(\gamma,p_{0,1})$, as measured by Mori *et al.*[10] at the same angle, showed the cross sections to be approximately equal over a wide energy range, but especially from $E_\gamma = 70$ to 100 MeV. This similarity is consistent with calculations incorporating two-body effects in the photoreaction process, such as by Gari and Hebach,[28] and by Cavinato *et al.*[29] It is also consistent with the predictions of the modified QDM by Schoch,[24] which predicts similar magnitudes for the $^{12}C(\gamma,n_0)$ and $^{12}C(\gamma,p_0)$ cross sections. The results, however, are inconsistent with a direct, single-nucleon knockout model of photon absorption, which predicts the cross section to be much smaller than that of (γ,p_0).

The data presented for the region of high missing energy provide new and important information that is complementary to the corresponding photoproton data of Mori *et al.*[10] and McGeorge *et al.*[9] The ^{12}C photoneutron cross section presented here is approximately equal to the ^{12}C photoproton cross section data mentioned above over the full missing energy range. This agreement, and the large cross section magnitude at high missing energy ($E_m > 40$ MeV), cannot be reconciled with a direct, single-nucleon knockout model. Conversely, calculations based on a QDM of photon absorption were found to account for the general shape and approximately 60% of the magnitude of the measured cross sections in the region of high missing energy. This level of agreement is reasonably good, considering the uncertainties in the parameters employed in the QDM calculations. This fairly successful application of the QDM to the photoneutron and photoproton cross sections studied here, indicates that the two-body effects of photoreactions can be roughly simulated by a QDM calculation. A more complete calculation, however, would treat final-state interactions in a more detailed fashion, in order to predict the relative importance of (γ,pn), (γ,p_0), and (γ,n_0) reactions.

To test more completely the predictions of models incorporating two-body effects in the photoreaction process, extensive angular-distribution data are required for the regions of both low and high missing energy. Until now, very little data have been available for the high missing energy region. However, with the advent of several new high-duty-factor accelerators and tagged-photon facilities, this energy region should become increasingly accessible. High resolution measurements, not only of the neutron and proton channels, but of correlated outgoing pairs are needed to provide more stringent test of the models.

ACKNOWLEDGMENTS

This work was supported under a grant from the Australian Research Grant Committee. One of the authors (P.D.H.) was supported financially by a University of Melbourne Postgraduate Scholarship, and another (G.J.O'K.) by a Commonwealth Post-Graduate Award.

*Present address: Nuclear Physics Laboratory, University of Illinois, Champaign, IL 61820.

[1]S. Boffi, C. Giust, and F. D. Pacati, Lett. Nuovo Cimento **32**, 381 (1981).

[2]S. Boffi, R. Cenni, C. Giusti, and F. D. Pacati, Nucl. Phys. **A420**, 38 (1984).

[3]D. J. S. Findlay and R. O. Owens, Phys. Rev. Lett. **37**, 674 (1976); D. J. S. Findlay and R. O. Owens, Nucl. Phys. **A292**, 53 (1977); D. J. S. Findlay *et al.*, Phys. Lett. **74B**, 305 (1978).

[4]L. R. B. Elton and A. Swift, Nucl. Phys. **A94**, 52 (1967).

[5]J. S. Levinger, Phys. Rev. **84**, 43 (1951).

[6]K. G. Dedrick, Phys. Rev. **100**, 58 (1955).

[7]J. L. Matthews *et al.*, Nucl. Phys. **A112**, 654 (1968); J. L. Matthews, MIT Lab. Nucl. Sci. Internal Report **112** (1967) (unpublished).

[8]H. Schier and B. Schoch, Nucl. Phys. **A229**, 93 (1974); H. Schier and B. Schoch, Lett. Nuovo Cimento **12**, 334 (1975).

[9]J. C. McGeorge *et al.*, Phys. Lett. B **179**, 212 (1986).

[10]K. Mori *et al.*, Lab. Nucl. Sci. Tohoku Univ. Report **18**, 225 (1985); T. Terasawa *et al.*, *ibid.* **18**, Suppl. 4, 12 (1985).

[11]M. Q. Barton and J. H. Smith, Phys. Rev. **95**, 573 (1954).

[12]H. Meyer, A. C. Odian, P. C. Stein, and A. Wattenberg, Phys. Rev. **95**, 576 (1954).

[13]A. Wattenberg, A. C. Odian, P. C. Stein, and H. Wilson, Phys. Rev. **104**, 1710 (1956).
[14]M. Q. Barton and J. H. Smith, Phys. Rev. **110**, 1143 (1958).
[15]P. C. Stein, A. C. Odian, A. Wattenberg, and R. Weinstein, Phys. Rev. **119**, 348 (1960).
[16]J. Garvey, B. H. Patrick, J. G. Rutherglen, and I. L. Smith, Nucl. Phys. **70**, 241 (1965).
[17]I. L. Smith, J. Garvey, J. G. Rutherglen, and G. R. Brooks, Nucl. Phys. **B1**, 483 (1967).
[18]O. A. P. Tavares, J. D. Pinheiro Filho, V. Di Napoli, J. B. Martins, and M. L. Terranova, Lett. Nuovo Cimento **27**, 350 (1980).
[19]S. Homma *et al.*, Phys. Rev. C **27**, 31 (1983); S. Homma *et al.*, Phys. Rev. Lett. **53**, 2536 (1984).
[20]M. W. Wade, M. K. Brussel, L. J. Koester, and J. H. Smith, Phy. Rev. Lett. **53**, 2540 (1984).
[21]A. Leprêtre *et al.*, Nucl. Phys. **A367**, 237 (1981).
[22]P. Carlos *et al.*, Nucl. Phys. **A378**, 317 (1982).
[23]M. Anghinolfi *et al.*, Nucl. Phys. **A457**, 645 (1986).
[24]B. Schoch, Phys. Rev. Lett. **41**, 80 (1978).
[25]B. Schoch *et al.*, Phys. Rev. C **22**, 2630 (1980); H. Göringer and B. Schoch, Phys. Lett. **109B**, 41 (1980); H. Göringer, B. Schoch, and G. Lührs, Nucl. Phys. **A384**, 414 (1982); B. Schoch and H. Göringer, Phys. Lett. **109B**, 11 (1982).
[26]B. Schoch, *Proceedings of the Fourth International Conference on Intermediate Energy Nuclear Physics,* San Miniato, Italy (World-Scientific, Singapore, 1983).
[27]M. R. Sené *et al.*, Phys. Rev. Lett. **50**, 1831 (1983); M. R. Sené *et al.*, Nucl. Phys. **A442**, 215 (1985).
[28]H. Hebach, A. Wortberg, and M. Gari, Nucl. Phys. **A267**, 425 (1976); M. Gari and H. Hebach, Phys. Rep. **72**, 1 (1981).
[29]M. Cavinato, M. Marangoni, P. L. Ottaviani, and A. M. Saruis, Nucl. Phys. **A373**, 445 (1982); M. Cavinato, M. Marangoni, and A. M. Saruis, Nuovo Cimento A **76**, 197 (1983); M. Cavinato, M. Marangoni, and A. M. Saruis, Nucl. Phys. **A422**, 237 (1984).
[30]S. Penner and J. E. Leiss, Phys. Rev. **114**, 1101 (1959).
[31]G. Manuzio, G. Ricco, M. Sanzone, and L. Ferrero, Nucl. Phys. **A133**, 225 (1969).
[32]H. G. Miller, W. Buss, and J. A. Rawlins, Nucl. Phys. **A163**, 637 (1971).
[33]J. L. Matthews, D. J. S. Findlay, S. N. Gardiner, and R. O. Owens, Nucl. Phys. **A267**, 51 (1976).
[34]D. J. S. Findlay and R. O. Owens, Nucl. Phys. **A279**, 385 (1977).
[35]D. J. S. Findlay, D. J. Gibson, R. O. Owens, and J. L. Matthews, Phys. Lett. **79B**, 356 (1978).
[36]J. Asai, J. J. Murphy II, and D. M. Skopik, Phys. Rev. C **21**, 469 (1980).
[37]M. J. Leitch *et al.*, Phys. Rev. C **31**, 1633 (1985).
[38]R. A. Schumacher *et al.*, Phys. Rev. C **33**, 50 (1986).
[39]T. Terasawa *et al.*, Nucl. Instrum. Methods **248**, 429 (1986).
[40]P. Sperr, H. Spieler, M. R. Maier, and D. Evers, Nucl. Instrum. Methods **116**, 55 (1974).
[41]L. J. Perkins and M. C. Scott, Nucl. Instrum. Methods **166**, 451 (1979).
[42]R. Kurz, University of California Report UCRL 11339 (unpublished) (1967); R. R. Doering, D. M. Patterson, and A. Galonsky, Phys. Rev. C **12**, 378 (1975).
[43]F. Partovi, Ann. Phys. (N.Y.) **27**, 79 (1964).
[44]M. P. De Pascale *et al.*, Phys. Lett. **119B**, 30 (1982).
[45]J. M. Cameron, Can. J. Phys. **62**, 1019 (1984).
[46]V. V. Verbinski *et al.*, Nucl. Instrum. Methods **65**, 8 (1968).
[47]Y. S. Horowitz, S. Mordechai, and A. Dubi, Nucl. Instrum. Methods **123**, 551 (1975).
[48]M. Drosg, Nucl. Instrum. Methods **105**, 573 (1972).
[49]R. Cenni and G. A. Rottigni, Lett. Nuovo Cimento **15**, 574 (1976).
[50]S. Boffi, Nuovo Cimento A **76**, 186 (1983); S. Boffi, C. Giusti, F. D. Pacati, and M. Rosa-clot, Nuovo Cimento A **76**, 685 (1983).
[51]S. Boffi, F. Capuzzi, C. Giusti, and F. D. Pacati, Nucl. Phys. **A436**, 438 (1985).
[52]K. Gottfried, Nucl. Phys. **5**, 557 (1958).
[53]C. W. de Jager, H. de Vries, and C. de Vries, At. Data Nucl. Data Tables **14**, 479 (1974).
[54]J. A. Jansen, R. Th. Peerdeman, and C. de Vries, Nucl. Phys. **A188**, 337 (1972).
[55]H. G. Carvalho *et al.*, Notas Fis. **17**, 4 (1971).
[56]M. Blann, B. L. Berman, and T. T. Komoto, Phys. Rev. C **28**, 2286 (1983).
[57]G. Jacob and Th. A. J. Maris, Rev. Mod. Phys. **38**, 121 (1966).